

Deformation Analysis of the Long-Period Stacking-Ordered Phase by Using Molecular Dynamics Simulations: Kink Deformation under Compression and Kink Boundary Migration under Tensile Strain

Ryosuke Matsumoto* and Masayuki Uranagase

Department of Mechanical Engineering and Science, Graduate School of Engineering, Kyoto University,
Kyoto 615-8540, Japan

The long-period stacking-ordered (LPSO) phase discovered in magnesium alloys is deformed upon the generation of a large number of unique deformation zones, which have no distinct orientation relationships at the deformation boundaries. These deformation zones are considered kink bands, but the mechanisms underlying their generation are not well understood. It has been suggested that the kink bands are responsible for the deformation of the LPSO phase, while simultaneously strengthening the material. In this study, the kink deformation process of the LPSO phase under compressive deformation was investigated through molecular dynamics (MD) simulations. The MD simulations showed that numerous prismatic (*a*) dislocations were nucleated first, which led to cross-slips towards various basal planes and caused kink deformation. This was followed by the nucleation and motion of a large number of basal dislocations, as well as kink deformations in tandem with the formation of kink bands, which occurred through another process. In addition, the individual dislocations were indistinguishable at kink boundaries. In other words, sharp boundaries were formed. Next, a simulation was performed that applied tensile strain to the model after the compressive deformation described above was implemented on it. This revealed that while kink boundaries with large misorientation angles intermittently migrated because of the tensile strain, the kink bands were not easily removed. [doi:10.2320/matertrans.MH201408]

(Received December 25, 2014; Accepted February 13, 2015; Published June 25, 2015)

Keywords: molecular dynamics, dislocation, long-period stacking-ordered structure, kinks, deformation

1. Introduction

Magnesium alloys that contain the long-period stacking-ordered (LPSO) phase in the alpha phase (Mg-LPSO) were recently discovered, with experiments indicating that they possess a high yield stress and reasonable ductility.^{1–5)} The LPSO phase is known to undergo deformations by generating numerous deformation boundaries that have no distinct orientation relationships under compressive deformation.^{6–9)} This deformation mode is believed to correspond to kink deformation, which was first discovered by Orowan during his compression tests on cadmium.¹⁰⁾ Even though this type of deformation is thought to be the underlying cause of the excellent mechanical properties of Mg-LPSO alloys, the mechanisms governing the kink deformations that occur in the LPSO phase are not well understood. For example, according to the mechanism proposed by Hess and Barrett,¹¹⁾ kink deformation occurs because of an array of edge dislocations on basal planes. However, the dislocation distances would have to be extremely short to form the high-angle boundaries that are experimentally observed. These boundaries are also believed to migrate easily in the cases where the kink boundaries are comprised of discrete edge dislocations. Furthermore, when kink boundaries with different bending directions are paired, which is referred to as a “kink band”, such kink boundaries are expected to annihilate each other upon load removal or tensile strain. However, the generation of kink boundaries and kink bands has been demonstrated experimentally to be responsible not only for deformations, but also for strengthening the material after their generation.^{12,13)}

We previously developed a single-element atomic model of the LPSO phase whose interactions were described by a smoothed Lennard–Jones (SLJ) potential, and subsequently performed deformation analysis on it using molecular dynamics (MD) simulations.¹⁴⁾ It was evident from the simulations that deformation twinning was strongly inhibited in the LPSO phase. Furthermore, the simultaneous application of compressive deformation in a direction parallel to the basal plane and shear deformation in the perpendicular direction generated deformation boundaries that had no distinct orientation relationships, i.e., kink boundaries. For such instances, pairs of edge dislocations were generated on the basal planes, originating from the numerous lattice defects that were caused by the migration of a pyramidal dislocation. However, the motion of the basal dislocations was strongly affected by the boundary conditions because of the limited dimensions of the simulation model.

In this paper, we employ a large-scale model to reduce the influence of artificial deformation constraints, and provide an analysis of the slip system acting during the kink deformation process of the LPSO phase. Furthermore, we discuss the results obtained from an examination of the resistance to kink boundary migration, which was performed by applying tensile strain to a model in which kink bands had been introduced.

2. Atomic Model and Calculation Conditions

The structure of the LPSO phase is that of a face-centered cubic (fcc) structure periodically inserted between hexagonal close packed (hcp) structures. It has been demonstrated that elements other than Mg become concentrated and reside in the fcc section.^{15–19)} The simulations presented in this paper

*Corresponding author, E-mail: matsumoto@solid.me.kyoto-u.ac.jp

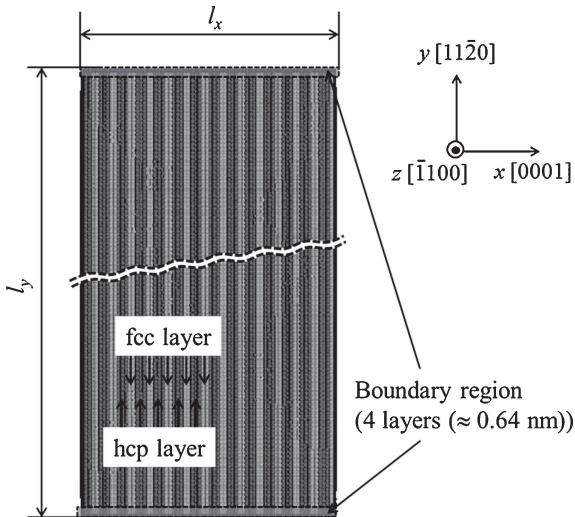


Fig. 1 The initial pillar-shaped structure of the LPSO model.

were focused on the influence of the characteristic stacking of fcc and hcp structures on the deformation behavior by utilizing the SLJ potential^{20,21)} for a single-element system, as in our previous study.¹⁴⁾

Deformation analysis was performed on a LPSO phase with a 10H (hexagonal) type stacking. The 10H-type stacking has the highest density of stacking faults (fcc section) among the reported stacking types.¹⁷⁾ The model used for this study had a threefold increase in length along the compression axis compared to that of the previous model¹⁴⁾ (Fig. 1). Periodic boundary conditions were not used and the model's dimensions were $l_x \times l_y \times l_z = 18.1 \times 95.4 \times 18.7$ nm, with 1,428,000 atoms. The crystal was arranged in such a way that the $[0001]$ (c -axis) was in the x -axis direction, the $[11\bar{2}0]$ (a -axis) in the y -axis direction, and the $[\bar{1}100]$ in the z -axis direction. The boundary regions were defined as the final four atomic layers at both ends in the y -axis direction, as indicated in Fig. 1; the motion of the atoms in the boundary region was constrained in the x - and y -directions. The time step, Δt , was 2 fs. The temperature was kept constant at 300 K by the velocity scaling method, which was used in all of the following calculations.

A relaxation calculation was performed first for 33 ps. During this calculation, the atomic velocities were reset every 6 ps to remove vibrations, and the size of the model was scaled such that the average stresses (σ_{xx} , σ_{yy} , σ_{zz}) were reduced to zero.

3. Analysis of Kink Deformation under Compressive Deformation

Once the relaxation calculation was performed, deformation was applied by assigning a displacement gradient equivalent to $\dot{\gamma}_{xy} = 1.414 \times 10^8 \text{ s}^{-1}$ and $\dot{\epsilon}_{yy} = -0.707 \times 10^8 \text{ s}^{-1}$ to all atoms in the model, while the motions of the atoms in the boundary regions were constrained.

Stress-strain curves for the deformation process are shown in Fig. 2. The deformation states for points (i) to (vi) of Fig. 2 are shown in Fig. 3. To visualize the atomic structure in Fig. 3, we first used common-neighbor analysis (CNA)²²⁾ to categorize the atoms according to the local structure. That

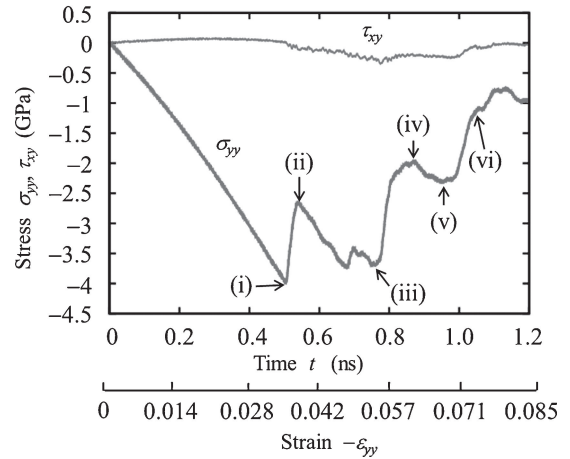


Fig. 2 Stress-strain curves for the compressive deformation.

is, each atom is classified as (a) an hcp-structured atom, (b) an fcc-structured atom, or (c) a defect atom that is neither an hcp- nor fcc-structured atom. For the hcp-structured atoms, we defined the c -axis at each atomic position using the positional relationships for the six second-neighbor atoms of the ideal hcp configuration and estimated the rotational angle, φ , of the c -axis around the z -axis. The hcp-structured atoms were then colored according to $|\varphi|$, with the fcc-structured atoms colored gray and defect atoms colored black. As can be seen in Fig. 2, the compressive stress rapidly decreases between the points marked (i) and (ii) ($t \approx 500$ ps), (iii) and (iv) ($t \approx 800$ ps), and (v) and (vi) ($t \approx 1050$ ps). Consequently, several lattice defects were generated at the bent boundaries, which are indicated by the arrows in Figs. 3(ii), (iv), and (vi). The misorientation angles at the bent boundaries are not consistent with one another, and thus, it is assumed that these are kink boundaries, which implies that the acting deformation mode is kink deformation. For the first two kink deformations, it is also evident that the deformation boundaries were formed independently. When the last kink deformation occurred, an increase in the misorientation angle (in mutually opposite directions) rapidly occurred at the two kink boundaries shown in the top part of Fig. 3(vi), and thus, a kink band was formed. It should be noted that deformation twinning occurs in hcp single crystals and conventional slip deformation occurs in fcc single crystals, as described in our previous paper,¹⁴⁾ and thus, the LPSO structure plays a key role in causing kink deformation.

The distribution of the slip system after the second kink deformation is shown in Fig. 4. Color was added to Figs. 4(B) and (C) according to the legend shown in Fig. 4(D), i.e., according to the relative displacement of two neighboring basal planes. The relative displacement is defined by $\mathbf{d}_+ - \mathbf{d}_-$, where \mathbf{d}_+ is the displacement of the basal plane on the right side (in the x -axis direction) and \mathbf{d}_- is the displacement of the intended atom. For the fcc structure, the $\{111\}$ plane, which is parallel to the basal plane of the hcp structure in the initial state, is also referred to as a “basal plane” for convenience. The positions of the external apex of the hexagon shown in Fig. 4(D) correspond to the displacement of $1\mathbf{b}$, where \mathbf{b} is the Burgers vector. Furthermore, the atoms that had either hcp or fcc structures in their initial states, and whose positional relationships with neighboring

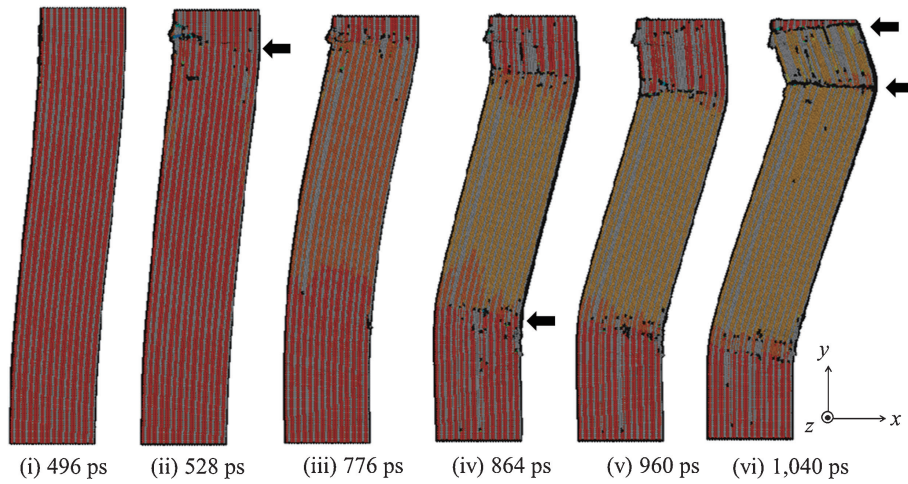


Fig. 3 Structural changes caused by the compressive deformation at the mid-plane ($z = l_z/2$). Atoms shown in black and gray are defect atoms (other than fcc- or hcp-structured atoms) and fcc-structured atoms, respectively. The hcp-structured atoms are colored according to the local c -axis direction, i.e., red and green indicate the angles between the projection vector of the c -axis on the x - y plane and x direction are 0° and 45° , respectively. Continuous RGB coloring is used for intermediate angles.

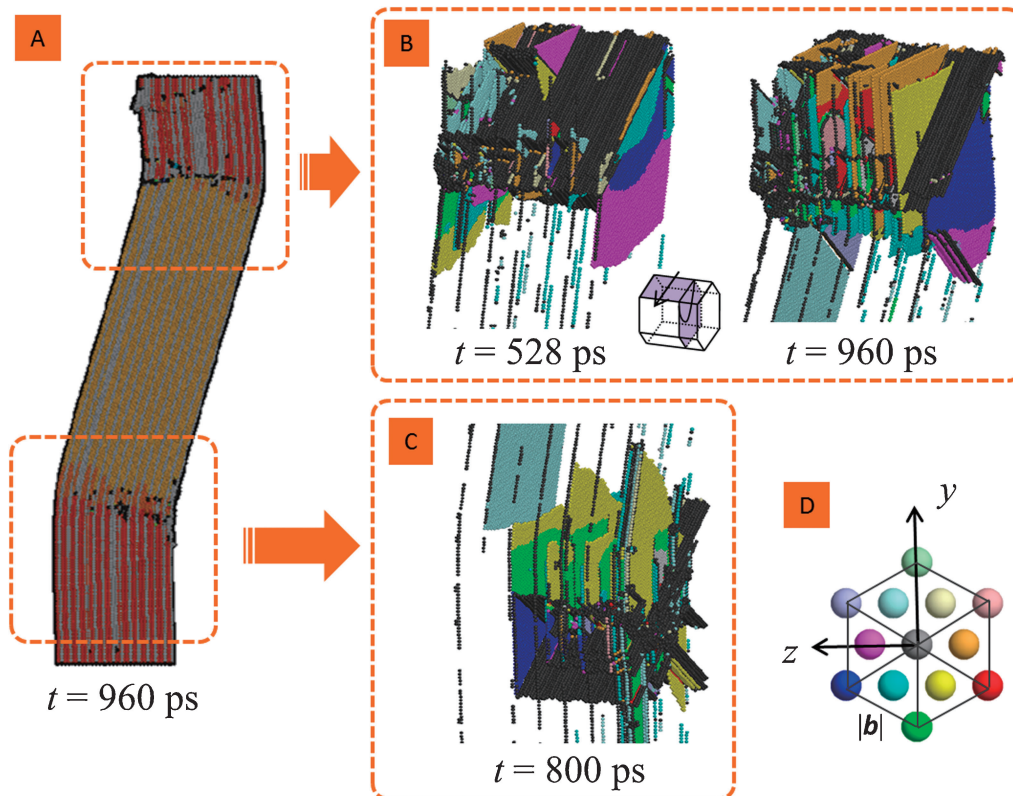


Fig. 4 Distribution of slipped planes after the first two kink deformations. (A) shows the entire model at $z = l_z/2$. (B) and (C) show the distribution of slipped planes in the upper and lower parts, respectively. (D) shows the color pattern used to depict the slip direction.

atoms inside the basal plane (six atoms) changed after deformation, are shown in black. This means that non-basal slips occurring between the planes are represented in black. The linear rows of atoms in the Figs. 4(B) and (C) result from a failure to determine the structures near the surface and they could not be removed. According to Fig. 4, negligible glide occurred at the center of the deformed model, which also reveals that the kink boundaries in the upper and lower sections were formed independently. Furthermore, it is evident that prismatic slips, as well as basal slips originating from the slipped prismatic planes, have occurred. This is

due to the cross-slips of many prismatic $\langle a \rangle$ dislocations ($\{10\bar{1}0\}\langle 11\bar{2}0 \rangle$), whose slip plane is inclined by 60° with respect to the compression axis, towards various basal planes. Thus, slips of $|1b|$ (indicated by blue and red in Fig. 4(D)) are caused by the motion of the basal dislocations with a Burgers vector of the prismatic $\langle a \rangle$ dislocations described above. The slips indicated by pink, orange, yellow, and light blue in Fig. 4(D) are then caused by the motion of partial dislocations coming from the prismatic $\langle a \rangle$ dislocations. The prismatic plane of the LPSO structure is bent in the fcc layer, as shown in Fig. 5. This means that it would be difficult for

edge dislocations to move on the prismatic plane and that screw dislocations with dislocation lines perpendicular to the viewing plane will occur, as indicated by the white arrows in Fig. 5. For such cases, it is believed that a cross-slip towards the basal plane is promoted because of the bent slip plane, and then the deformation mechanism described above occurs.

Details of the deformation behavior of the upper section of the model are shown in Fig. 6. The coloring used in Fig. 6(A) is same as that of Fig. 3. Based on the CNA analysis, only defects are shown in Fig. 6(B) and the distribution of the slipped planes is shown in Fig. 6(C). To show the slips on the basal plane clearly, non-basal slips that were black in Figs. 4(B) and (C) are not shown in Fig. 6(C). The first two kink deformations occur through the aforementioned cross-slip mechanism, but the third kink deformation that occurs at $t \approx 1050$ ps is caused by a large quantity

of basal dislocations that form between the two kink boundaries in the upper section. Consequently, the misorientation angle at the boundaries increases rapidly between $t = 960$ ps and 1040 ps (Fig. 6(A)). The source of such basal dislocations is not clear at this stage, but the kink boundary generated earlier is believed to play a vital role because an extremely high level of stress is required to produce dislocation pairs in perfect crystals.^{23–25} The distribution of the slipped planes after the kink deformation is shown in Fig. 7. Seventy basal planes exist in this cross section, which are indicated by the dotted line in Fig. 7, and of which 43 planes have slipped. As a result, there is a high density of dislocations inside the boundary, as is evident from

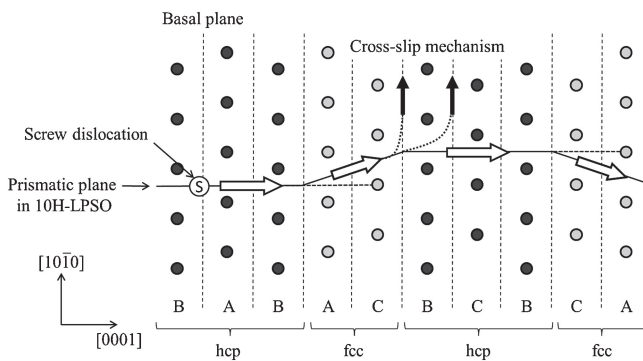


Fig. 5 The prismatic plane in the LPSO structure and the screw dislocation motion.

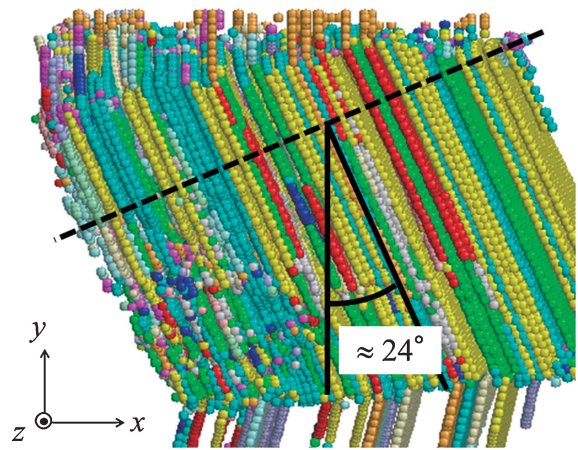


Fig. 7 Distribution of the basal slips in the kink band generated in the upper part of the model ($z = l_z/2$, $t = 1120$ ps).

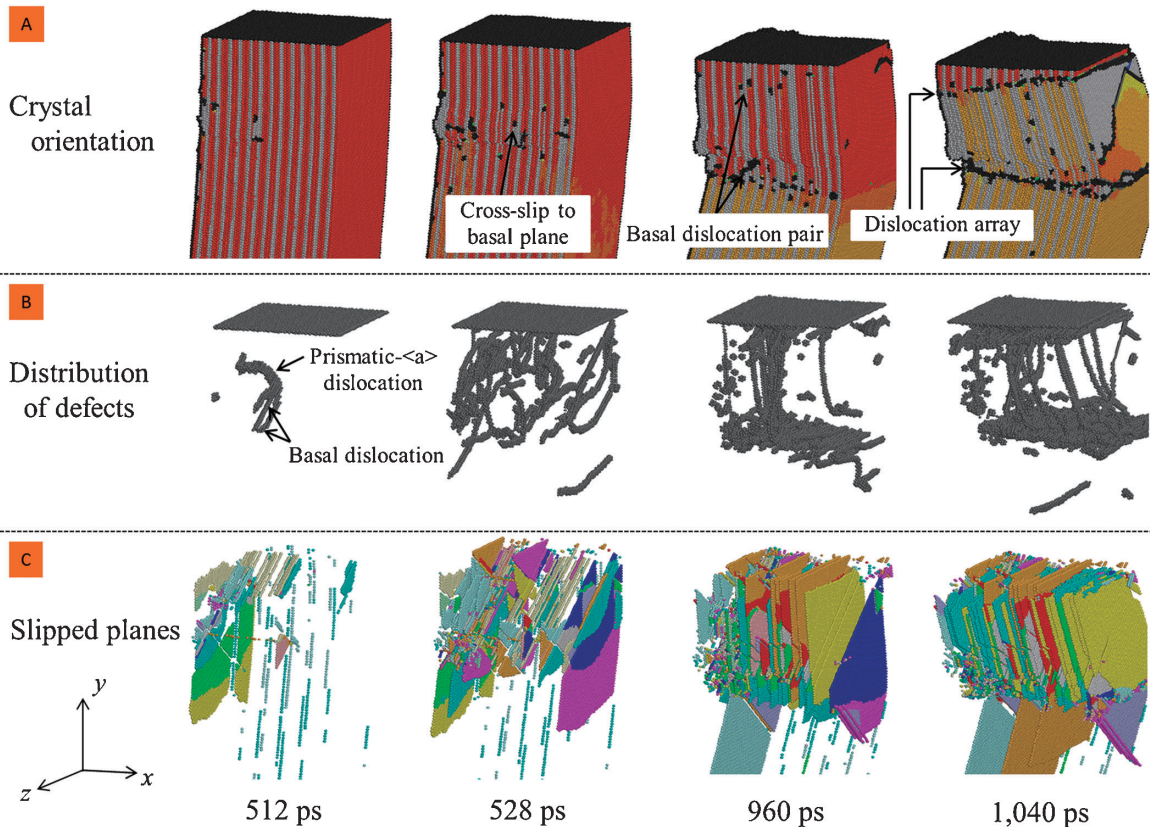


Fig. 6 Detailed structural changes in the upper part of the model. (A) shows the crystal orientation and defect distribution. (B) only shows defect atoms that constitute neither fcc nor hcp structures. (C) shows the distribution of the basal slips.

Fig. 6(A), and the individual dislocations are indistinguishable. Furthermore, because multiple dislocation motions on a single slip plane were scarce, no dislocation pile-ups were observed at the kink boundaries. These features are in agreement with TEM observations.^{7,26} The misorientation angle of the kink boundary at the top of the model is about 24° . In contrast, the sum of the slip vectors contributing to the rotation around the z -axis (along the dotted line shown in Fig. 7) is $25b$. Assuming that this is distributed evenly at the boundary, the calculated misorientation angle is nearly identical to the misorientation angle described above. This result clearly indicates that the kink boundary is formed by basal dislocations, and the contribution from edge dislocations increases the misorientation angle.

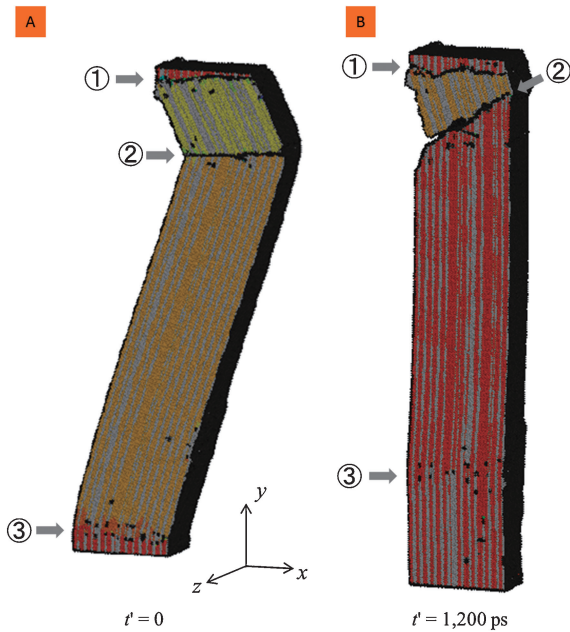


Fig. 8 Atomic structure of the model at the mid plane ($z = l_z/2$). (A) and (B) show the structure after relaxation ($t' = 0$) and after reverse deformation ($t' = 1200$ ps), respectively.

4. Analysis of the Migration Behavior of Kink Boundaries under Tensile Strain

The velocities of all atoms were reset after the deformation conditions described in Section 3 ($t = 1200$ ps) were applied and a relaxation calculation was performed for 63 ps with the same conditions described in Section 2. The time after the relaxation was set to $t' = 0$. The appearance of the model after this relaxation is shown in Fig. 8(A). Next, a reverse deformation (opposite to that of the previous section) of $\dot{\gamma}_{xy} = -1.414 \times 10^8 \text{ s}^{-1}$, $\dot{\epsilon}_{yy} = 0.707 \times 10^8 \text{ s}^{-1}$ was applied.

The model after the deformation ($t' = 1200$ ps) is shown in Fig. 8(B). The visualization method is same as that used for Fig. 3, and the numerals 1, 2, and 3 indicate the positions of kink boundaries before and after deformation. At this time, the boundary regions have reverted to their initial positions at $t = 0$. However, it is evident from Fig. 8(B) that many dislocations and kink boundaries remain after the application of reverse deformation.

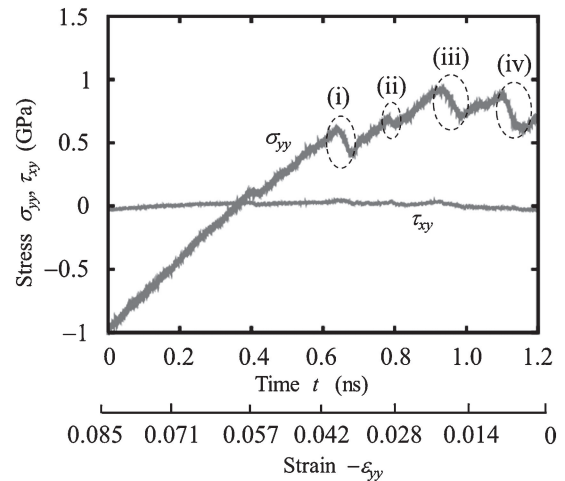


Fig. 9 Stress-strain curves during reverse deformation.

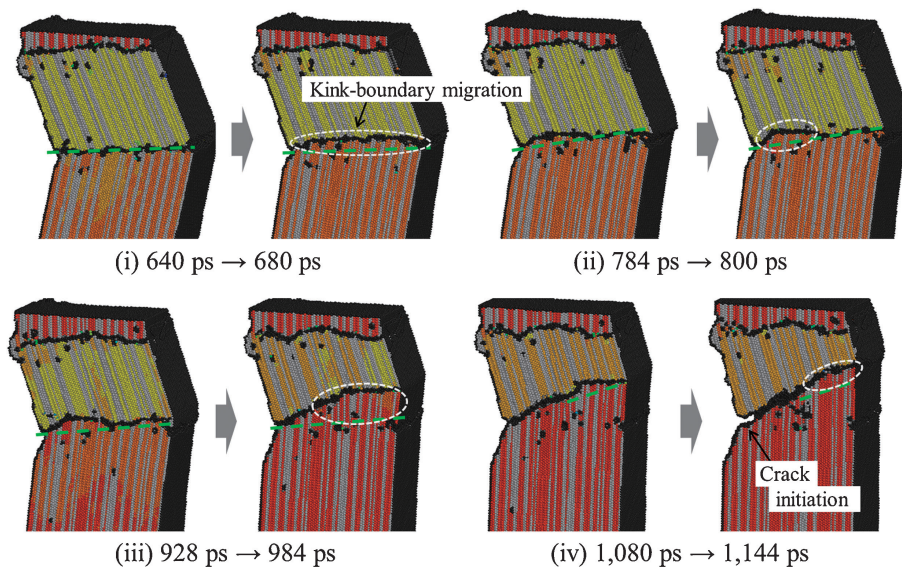


Fig. 10 Structural changes during reverse deformation. The deformation state at the mid-plane is shown ($z = l_z/2$). (i), (ii), (iii), and (iv) show the structural changes during the stress reductions indicated in Fig. 9. The green dotted lines indicate the same position before and after the migration of the kink boundary.

Stress–strain curves for the reverse deformation process are shown in Fig. 9; rapid decreases in the tensile stress are indicated by points (i) to (iv). The structural changes for (i) to (iv) are shown in Fig. 10. The kink band in the upper section of the model is magnified in Fig. 10, with the locations of migrations marked with dotted circles. It is evident from Figs. 9 and 10 that the kink boundary intermittently migrates in conjunction with the rapid decrease in stress. Furthermore, the kink boundary is not flat like a twin boundary and it is evident that it bends under a load.

As the analysis was performed using a MD simulation, the deformation rate is fast, and therefore, a quantitative discussion is difficult. However, it is evident that about half of the stress required for the generation of these kink boundaries (from points (v) to (vi) in Fig. 2) would be necessary for a kink boundary with a large misorientation angle to migrate. Though not illustrated here, kink boundary 3 in Fig. 8 (with a small misorientation angle) migrated smoothly upon structural relaxation and the application of tensile strain. This could be attributed to the fact that individual dislocations do not exist within the boundary when the misorientation angle of the kink boundary increases. These dislocations cause a variety of reactions and restructure as a sharp deformation boundary. Therefore, the mobility of the kink boundary is reduced as the misorientation angle increases,²⁷⁾ which is believed to contribute to material strengthening, much like ordinary grain boundaries.

5. Conclusions

Analysis of the kink deformation and migration of kink boundaries in the LPSO phase was performed with MD simulations. The following results were obtained:

- (1) Some deformation modes that lead to kink deformation, depending on the dislocation motions, were confirmed to exist.
- (2) Kink deformation was found to occur when numerous prismatic $\langle a \rangle$ dislocations caused cross-slips towards the basal planes.
- (3) Following the prismatic $\langle a \rangle$ dislocations described above, a kink band is formed as a large number of edge dislocations are generated on the basal plane. In this case, the dislocations are densely packed at the kink boundary. While it was not possible to verify the source of the basal dislocations, the lattice defects previously introduced by the prismatic $\langle a \rangle$ dislocations are believed to play an important role.
- (4) The migration of a kink boundary requires considerable stress because individual dislocations do not exist within the boundary when the misorientation angle increases. Thus, the kink bands are not easily removed, and they contribute to the strengthening of the LPSO phase.

Acknowledgements

This work was partially supported by a Grant-in-Aid for Scientific Research on Innovative Areas “Synchronized Long-Period Stacking-Ordered Structure” from the Ministry of Education, Culture, Sports, Science and Technology (MEXT) of Japan.

REFERENCES

- 1) Y. Kawamura, K. Hayashi, A. Inoue and T. Masumoto: *Mater. Trans.* **42** (2001) 1172–1176.
- 2) S. Yoshimoto, M. Yamasaki and Y. Kawamura: *Mater. Trans.* **47** (2006) 959–965.
- 3) Y. Kawamura and M. Yamasaki: *Mater. Trans.* **48** (2007) 2986–2992.
- 4) K. Hagihara, A. Kinoshita, Y. Sugino, M. Yamasaki, Y. Kawamura, H. Y. Yasuda and Y. Umakoshi: *Acta Mater.* **58** (2010) 6282–6293.
- 5) M. Yamasaki, K. Hashimoto, K. Hagihara and Y. Kawamura: *Acta Mater.* **59** (2011) 3646–3658.
- 6) T. Itoi, K. Takahashi, H. Moriyama and M. Hirohashi: *Scr. Mater.* **59** (2008) 1155–1158.
- 7) K. Hagihara, N. Yokotani and Y. Umakoshi: *Intermetallics* **18** (2010) 267–276.
- 8) X. H. Shao, Z. Q. Yang and X. L. Ma: *Acta Mater.* **58** (2010) 4760–4771.
- 9) K. Hagihara, M. Honnami, R. Matsumoto, Y. Fukusumi, H. Izuno, M. Yamasaki, T. Okamoto, T. Nakano and Y. Kawamura: *Mater. Trans.* **56** (2015) 943–951.
- 10) E. Orowan: *Nature* **149** (1942) 643–644.
- 11) J. B. Hess and C. S. Barrett: *Trans. Am. Inst. Min. Metall. Eng.* **185** (1949) 599–606.
- 12) T. Morikawa, K. Kaneko, K. Higashida, D. Kinoshita, M. Takenaka and Y. Kawamura: *Mater. Trans.* **49** (2008) 1294–1297.
- 13) M. Hirano, M. Yamasaki, K. Hagihara, K. Higashida and Y. Kawamura: *Mater. Trans.* **51** (2010) 1640–1647.
- 14) R. Matsumoto, M. Uranagase and N. Miyazaki: *Mater. Trans.* **54** (2013) 686–692.
- 15) E. Abe, Y. Kawamura, K. Hayashi and A. Inoue: *Acta Mater.* **50** (2002) 3845–3857.
- 16) E. Abe, A. Ono, T. Itoi, M. Yamasaki and Y. Kawamura: *Philos. Mag. Lett.* **91** (2011) 690–696.
- 17) D. Egusa and E. Abe: *Acta Mater.* **60** (2012) 166–178.
- 18) K. Kishida, H. Yokobayashi, H. Inui, M. Yamasaki and Y. Kawamura: *Intermetallics* **31** (2012) 55–64.
- 19) M. Yamasaki, M. Matsushita, K. Hagihara, H. Izuno, E. Abe and Y. Kawamura: *Scr. Mater.* **78–79** (2014) 13–16.
- 20) R. Matsumoto and N. Miyazaki: *Scr. Mater.* **59** (2008) 107–110.
- 21) R. Matsumoto and M. Nakagaki: *Modell. Simul. Mater. Sci. Eng.* **14** (2006) S47–S54.
- 22) J. D. Honeycutt and H. C. Andersen: *J. Phys. Chem.* **91** (1987) 4950–4963.
- 23) M. Uranagase, S. Kamigaki, R. Matsumoto and N. Miyazaki: *Mater. Trans.* **54** (2013) 680–685.
- 24) M. Uranagase, S. Kamigaki and R. Matsumoto: *J. Soc. Mater. Sci. Jpn.* **63** (2014) 194–199.
- 25) M. Uranagase and R. Matsumoto: *Phys. Rev. B* **89** (2014) 224103.
- 26) H. Gao, K. Ikeda, T. Morikawa, K. Higashida and H. Nakashima: *Mater. Trans.* **54** (2013) 632–635.
- 27) Y. Huang, F. J. Humphreys and M. Ferry: *Acta Mater.* **48** (2000) 2543–2556.